Journal of Advanced Ceramics
2024, **13**(10): 1523–1534
https://doi.org/10.26599/JAC.2024.9220953

Research Article

Microwave-absorbing functionalization of $LaMgAl_{11}O_{19}$ composite thermal barrier coatings by atmospheric plasma spraying

Binglin Zou[1,✉], Yongqiu Zhang[1], Ying Wang[1], Xueqiang Cao[2,✉]

[1] *State Key Laboratory of Rare Earth Resources Utilization, Changchun Institute of Applied Chemistry, Chinese Academy of Sciences, Changchun 130022, China*
[2] *State Key Laboratory of Silicate Materials for Architectures, Wuhan University of Technology, Wuhan 430070, China*

Received: January 28, 2024; Revised: June 28, 2024; Accepted: August 5, 2024

Abstract: Thermal protection of the hot-end components of ultra-high-flying vehicles requires the microwave absorption of thermal barrier coating (TBC). In this work, the microwave-absorbing functionalization of $LaMgAl_{11}O_{19}$ (LMA) TBC was successfully realized by adding FeSiAl (FSA) absorber to the LMA thermal barrier ceramic matrix to adjust electromagnetic parameters. Due to the formation of the layered lamellae structure during atmospheric plasma spraying (APS), LMA–FSA composite TBCs have better electromagnetic wave (EMW) absorbing properties than feed powder. EMW absorption of TBCs is mainly controlled by the magnetic loss, and the natural resonance is the main mechanism of magnetic loss. TBCs exhibit a minimum reflection loss (RL) value of −13.4 dB, and effective absorption bandwidth (EAB) of RL < −10 dB is up to 3.11 GHz at a simulated thickness of 2 mm. Phase and structure stability of the TBCs and microwave absorption property could be relatively well preserved even after heat treatments at 600–1000 °C for 3–50 h. Thermal conductivity of the LMA–FSA composite TBCs with FSA contents of 30–50 wt% are about 2.84–3.05 $W \cdot m^{-1} \cdot K^{-1}$ at 800 °C. LMA–FSA composite TBCs with heat-resistant, heat-insulation, and EMW absorbing properties might find attractive potential applications in the thermal protection for the light alloy hot-end components in civil and military industry.

Keywords: thermal barrier coating (TBC); atmospheric plasma spraying (APS); microwave absorption; electromagnetic wave (EMW); thermal conductivity

1 Introduction

Thermal barrier coating (TBC) has the function of heat-resisting and heat-insulating at high temperatures because of its low thermal conductivity and high melting point [1]. TBC can be used not only for the thermal protection of the Ni-based superalloy above 1200 °C [1,2], but also for the thermal protection of light alloys, including magnesium alloy, aluminum alloy, and titanium alloy at relatively low temperatures [3–5]. As known, the maximum service temperature of the advanced aviation titanium alloy (e.g., TA15) is less than 550 °C, and that of the magnesium alloy and aluminum alloy is even generally less than 350 °C, so it is a good way to use TBCs on the light alloys when the temperature is more than the maximum service temperature [3–5].

Electromagnetic wave (EMW) absorbing material can not only endow the weapon equipment with radar stealthy performance to improve the penetration ability but also reduce EMW pollution and protect people from EMW harm, and therefore EMW absorption materials have very urgent needs [6,7]. Currently, EMW absorbing materials have two types of structural absorbing materials and microwave absorbing coatings, and the latter attracts more attention due to the advantages of thin-thickness, light-weight, and a much wider range of applications [8]. Compared with the magnesium alloy and aluminum alloy, the titanium alloy is a better structural material for the hot-end components of high-speed aircraft due to the relatively higher melting point, specific strength, and thermal stability [3]. In the future, the working temperature of the titanium alloy hot-end components of ultra-high-flying vehicles may reach 550–1000 °C, and so the requirement of high-temperature resistance, heat insulation, and electromagnetic stealth for TBC is put forward in order to avoid being detected by the radar and improve the battlefield survivability of weapons. However, as far as the authors know, TBC ceramic materials developed at present have no EMW absorption, and TBCs cannot perform radar stealth for the titanium alloy hot-end components. It is an urgent research direction to realize the microwave absorbing functionalization of TBCs for the light alloys, especially for the titanium alloy.

Atmospheric plasma spraying (APS) is one of the important preparation methods for TBCs [3–5]. Coincidentally, APS was also widely used to prepare EMW absorbing coatings, which exhibited merits of simple process, high efficiency, cost-effectiveness, and excellent adhesive strength and significantly promoted the development of EMW absorbing materials [9–15]. It is agreed that the ceramic composites composed of microwave absorbing agent and ceramic matrix could better satisfy the absorption characteristics of "light, thin, wide, and strong", in which the function of the absorbent is to attenuate and dissipate EMW and that of the ceramic matrix is to realize impedance matching [16–18]. Over the past decade, studies have shown that APS radar absorbing coatings containing alumina ceramic matrix and absorbents such as $LaSrMnO_3$ [19], Ti_4O_7/carbon nanotubes [8],

✉ Corresponding authors.
E-mail: B. Zou, zoubinglin@ciac.ac.cn;
X. Cao, xcao@whut.edu.cn

B_4C [9], FeCrAl [20,21], NiCrAlY [22], and FeSiAl/flake graphite [23] significantly gave rise to the desired EMW absorption property to reduce electromagnetic radiation. Inspired by this, APS of thermal barrier ceramic composites containing absorbent is an effective method to realize the microwave-absorbing functionalization of TBC. Considering that TBC materials are restricted by some basic requirements such as low thermal conductivity, high-temperature resistance, and phase stability during APS [24], the choice of absorbent for TBC must have relatively low thermal conductivity and good high-temperature stability.

At present, the absorbing agents mainly include Fe-, Co-, and Ni-based alloys, ferrites, conductive polymers, carbon materials, and dielectric ceramics [7]. According to the loss mechanism, the absorbing agents can be divided into the electrical loss type, such as graphite, carbon fiber, and carbon nano-materials absorbents; magnetic loss type, such as ferrite, iron-based alloys, and MoS_2 absorbents; and dielectric loss type, such as $BaTiO_3$, transition metal carbides/borides, and SiC ceramics absorbents [6,7,25–30]. Among these absorbing agents, one of the most likely absorbents to meet the basic requirements of TBC materials is iron-based alloys. Bobzin *et al.* [31] reported that the iron-based coatings with amorphous structure deposited by APS might be the next generation of TBCs for the low-temperature systems. Moreover, microwave coatings with wider absorption bandwidth and less thicknesses are required [17,21,23,26,29]. Compared with the dielectric materials, the magnetic absorbents have higher loss efficiency per unit thickness, so introducing the magnetic absorbent into coating can effectively reduce the coating thickness [17,30]. Up to now, the magnetic absorbent of the iron-based alloy i.e., FeSiAl (FSA), has significantly attracted much interest in microwave absorbing materials due to its high permeability, matched permittivity, and good thermal stability [23,32–36]. In addition, FSA magnetic absorbing agent is also one of the best potential absorbing coating materials for the thermal protection of light alloys. Therefore, FSA alloy was chosen as the absorbent of TBCs in this study.

Compared with the other ceramic TBCs such as yttria-stabilized zirconia (YSZ) and rare earth zirconate and cerate, $LaMgAl_{11}O_{19}$ (LMA) ceramic TBC by APS not only has the unique amorphous phase and plate-like grains, but also has the relatively low thermal conductivity and anti-oxygen permeability, and therefore LMA ceramics are one of the most promising TBC materials and heat-insulation, heat-resistance, and thermal shock resistance of LMA TBC are better [24,37–42]. In this work, in order to examine the possibility of microwave-absorbing functionalization of TBCs, LMA composite TBCs were prepared by APS via adding FSA absorbent to LMA ceramic matrix. Microstructure, EMW absorption, and thermodynamic properties of LMA ceramic composite powder and TBCs were investigated in detail. It is expected that this study could promote the development of heat-resistant, heat-insulation, and radar stealth TBCs, which may find potential applications in the thermal protection of light alloys, especially for the titanium alloy hot-end components of ultra-high-flying vehicles in the future.

2 Experimental

Commercial FSA powder with a particle size of 500-mesh was purchased from Hebei Huazuan Alloy Welding Material Co., Ltd., China, with a nominal composition of 9.2–9.7 wt% Si, 5.2–5.6 wt% Al, ≤ 0.3 wt% O, and Bal. Fe. LMA was synthesized by solid-state reaction at 1600 °C for 12 h using the powder mixture of La_2O_3, MgO, and Al_2O_3 (all purities > 99.9 wt%) with a mole ratio of 1:2:11. LMA powder with particle size less than 5 m was obtained by wet-milling of the produced LMA product for 72 h using zirconia balls (5–20 mm in diameter; Guangdong Drient Zirconic Industry Sci & Tech Co., Ltd., China). LMA–FSA powder mixtures with FSA contents of 30, 40, and 50 wt% were subjected to ball milling for 2 h with proper additions of deionized water, gum arabica, tri-ammonium citrate, and zirconia balls, respectively, followed by spray granulation of the obtained suspensions using the spray granulator (SFOC-16, Shanghai Ohkawara Dryers Co., Ltd., China). The ball milling speed used in this study was 150 r·min^{-1}, and LMA–FSA powder can be well mixed by ball milling for 2 h. It should be pointed out that effect of ball milling time on the microwave absorbing properties of TBCs is not obvious (Fig. S1 in the Electronic Supplementary Material (ESM)). The obtained agglomerate powder was sieved by the vibrating screens to collect those with particle sizes of 20–100 μm, which had good flowability and were used as feed powder for APS. LMA ceramic composite feed powder was plasma sprayed on the graphite substrates by APS using a Sulzer Metco plasma spraying unit with an F4-MB gun. Substrates were properly grit blasted with alumina sand prior to APS. Main plasma spraying parameters are presented in Ref. [17]. The thickness of coatings was about 2 mm, and the coatings were easily removed from the substrates using the wallpaper knife to obtain separate coating samples for the subsequent experimental tests.

Phase composition of the feed powder and coatings was identified by an X-ray diffractometer (XRD; D8 Advance diffractometer, Bruker, Germany; Cu Kα radiation, λ = 0.15406 nm) at 6 (°)·min^{-1} from 20° to 80°. Microstructures of the feed powder and coatings were observed by a scanning electron microscope (SEM; JSM-5310, HITACHI Company, Japan, or XL-30 ESEM FEG, Micro FEI Philips, USA) equipped with an energy-dispersive X-ray spectrometer (EDS; Link-ISIS, Oxford, UK). All coatings for cross-section analysis were firstly embedded in transparent epoxy resin and then cut by low-speed saw and polished with diamond pastes. Thermal expansion behavior of coatings was investigated by using a dilatometer (DIL 402 C, Netzsch, Germany) at a heating rate of 3 K·min^{-1} in air. Thermal diffusivity measurements were investigated using a laser flash apparatus (Port Washington THETA, NETZSCH Company, Germany) at a heating rate of 10 K·min^{-1} in argon. A vibrating sample magnetometer (VSM; Lakeshore 7410, Quantum Design Company, USA) was used to study the magnetic properties of the feed powder and coatings. The coatings were ground into granular powder (Fig. S2 in the ESM) and mixed with paraffin to prepare samples for microwave absorption tests. The powder samples of the feed powder and coatings were all mixed with paraffin wax at a mass ratio of 4:1 and compacted into the toroidal shape (ϕ_{out} = 7.00 mm, ϕ_{in} = 3.04 mm), and then electromagnetic parameters were measured by a vector network analyzer (VNA; Agilent N5234A, Keysight technology Co., Ltd., China) using the coaxial line method at the frequency range of 2–18 GHz. It is worth noting that the paraffin wax content has a significant effect on the dielectric constant (Fig. S3 in the ESM), and the content of paraffin wax used in this study was reasonably determined as 20 wt% in order to facilitate the comparative study of microwave absorbing properties. The relative complex permittivity (ε_r) and permeability (μ_r) were determined by using the electromagnetic parameters according to Eqs. (1) and (2) [7,17]:

$$\varepsilon_r = \varepsilon' - j\varepsilon'' \quad (1)$$

$$\mu_r = \mu' - j\mu'' \quad (2)$$

where j means that the permittivity and permeability are complex; ε' and ε'' are the real and imaginary parts of permittivity, respectively; μ' and μ'' are the real and imaginary parts of permeability, respectively. Dielectric loss tangent ($\tan\delta_\varepsilon$) and magnetic loss tangent ($\tan\delta_\mu$) were calculated according to Eqs. (3) and (4) [7,17]:

$$\tan\delta_\varepsilon = \varepsilon''/\varepsilon' \quad (3)$$

$$\tan\delta_\mu = \mu''/\mu' \quad (4)$$

For a given frequency and sample thickness, reflection loss (RL) was determined according to Eqs. (5) and (6) based on the transmission-line theory and meatal back-panel model, and attenuation constant (α) was calculated according to Eq. (7) [30,43]:

$$RL = 20\log\left|(Z_{in} - Z_0)/(Z_{in} + Z_0)\right| \quad (5)$$

$$Z_{in} = Z_0\sqrt{\mu_r/\varepsilon_r} \times \tanh\left(j2\pi fd\sqrt{\mu_r\varepsilon_r}/c\right) \quad (6)$$

$$\alpha = \sqrt{2}\pi f/c \times\sqrt{(\mu''\varepsilon'' - \mu'\varepsilon') + \sqrt{(\mu''\varepsilon'' - \mu'\varepsilon')^2 + (\mu''\varepsilon' - \mu'\varepsilon'')^2}} \quad (7)$$

where Z_{in} is the input characteristic impedance at the interface between atmosphere and absorber; Z_0 is the impedance of free space; f is the frequency; d is the thickness of sample; c is the velocity of light (3×10^8 m·s^{-1}). Effective absorption bandwidths (EABs) are defined by the frequency range with RL value smaller than −10 dB (comparable to 90% microwave energy absorption) or smaller than −5 dB (comparable to 70% microwave energy absorption) [28].

3 Results and discussion

3.1 Microstructure of powder and coatings

Morphologies of the produced LMA powder and FSA raw powder are shown in Figs. 1(a) and 1(b), respectively. It can be seen that LMA powder is typically plate-like with a particle size of less than 5 μm [40,41], and FSA raw powder is spherical with a particle size of less than 25 μm. TEM and HRTEM images for FSA raw powder (Figs. 1(c) and 1(d)) indicate that no obvious alumina film is found on the surface of FSA particles. However, alumina film with a thickness of approximately 8 nm is observed on the surface of FSA powder preheated at 700 °C for 6 h from the HRTEM image (Fig. 1(e)). Moreover, the elements of Fe, Si, Al, and O are uniformly distributed on the surface of FSA particles from the SEM image and element mappings (Fig. 1(f)). It is obvious that alumina film is formed on the surface of the pretreated FSA particles. In this study, FSA powder was directly used to spray granulation and APS without pretreatment. Figure 1(g) shows XRD patterns of FSA raw powder, FSA feed powder, and FSA coating. Only the diffraction peaks of $Al_{0.3}Fe_3Si_{0.7}$ phase (PDF#45-1206) appear, and no other oxidation products, such as Al_2O_3, are detected, implying that FSA powder was not oxidized obviously during the processes of spraying granulation and APS. Figures 1(h) and 1(i) show SEM images of LMA–FSA composite feed powder with FSA contents of 30 and 50 wt%, respectively. When the content of FSA is low, such as 30 wt%, FSA particles are almost wrapped by LMA particles after spray granulation, and only the spherical agglomerated composite particles marked with blue arrows are observed (Fig. 1(h)). With FSA content increasing to 50 wt%, a number of single FSA particles marked with yellow arrows and agglomerated FSA particles marked with red arrows are also observed in the feed powder (Fig. 1(i)). The typical SEM image of the crushed LMA–FSA feed powder (Fig. S4 in the ESM) shows that the sizes of the plate-like LMA particles and spherical FSA particles still remain less than 5 and 25 μm, respectively.

Figures 2(a) and 2(b) show XRD patterns of LMA–FSA feed powder and coatings with different FSA contents, respectively. As indicated, in addition to the main phases of LMA (PDF#26-0873) and FSA (PDF#45-1206), a small amount of impurity $LaAlO_3$ (PDF#31-0022) appeared, which is a metastable phase during synthesis of LMA [40]. Phase compositions of coatings are the same as those of the corresponding feed powder, implying that the feed powder has good phase stability during APS process. The diffraction peaks of coatings become relatively weak and broad as compared to those of feed powder, which should result from the formation of amorphous phase in the coatings [37–39]. The molten droplets solidify too quickly to crystallize during APS process, so the amorphous phase is formed [38].

Figure 3(a) shows the typical morphology of plasma-sprayed deposits for the individual particles of LMA–FSA composite feed powder. During APS process, the feed powder particle first melts and impacts the substrate and then spreads and forms a flat sheet deposit (Fig. 3(a)). With the continuous accumulation of the flat sheet deposits, the coating with the layered lamellae structure is fabricated. Figures 3(b) and 3(c) show the typical microstructures on the surface and cross-section of LMA–FSA composite TBC with 30 wt% FSA, respectively. As indicated, the coating surface is composed of molten deposits formed by fully spreading droplets of fully melted particles and partially melted deposits formed by partially melted particles. The fully and partially molten deposits pile up layer by layer, so the cross-section of TBC shows the typical layered lamellae structure together with some pores. Figure 3(d) shows the microstructure on the cross-sectional of LMA–FSA composite TBC with 50 wt% FSA. The single and agglomerated FSA particles in the feed powder with high FSA content (Fig. 1(i)) are easier to flatten during APS because of the lower melting point of FSA, and thus form the layered lamellas with a relatively large spread area (Fig. 3(d)), which is beneficial to improve the EMW absorbing properties of TBC, as will be mentioned below.

Figure 4(a) shows SEM images and the corresponding EDS mapping analysis of elements on the cross section of LMA–FSA composite coating with 40 wt% FSA. It can be seen that the elements of Fe and Si are distributed in the gray–white area, while the elements of La, Mg, and O are distributed in the gray–black area, indicating that the gray–white area is FSA phase, and the gray–black area is LMA phase. The gray–white FSA phase is distributed relatively evenly in the gray–black LMA ceramic matrix, with clear phase boundaries. It is worth mentioning that the mapping distribution of oxygen element was not detected in the gray–white FSA region, indicating that FSA did not undergo obvious oxidation during APS process. LMA–FSA composite coating was ground into powder and observed by TEM and HRTEM. As shown in Fig. 4(b), LMA and FSA phases are indeed distributed in the coating, and the phase boundaries are clear. By the lattice spacing analysis in Fig. 4(c), the corresponding lattice stripes of (101) and (114) for LMA phase, (220) for FSA phase, and (110) for $LaAlO_3$ are found, which is consistent with the phase analysis of XRD in Fig. 2.

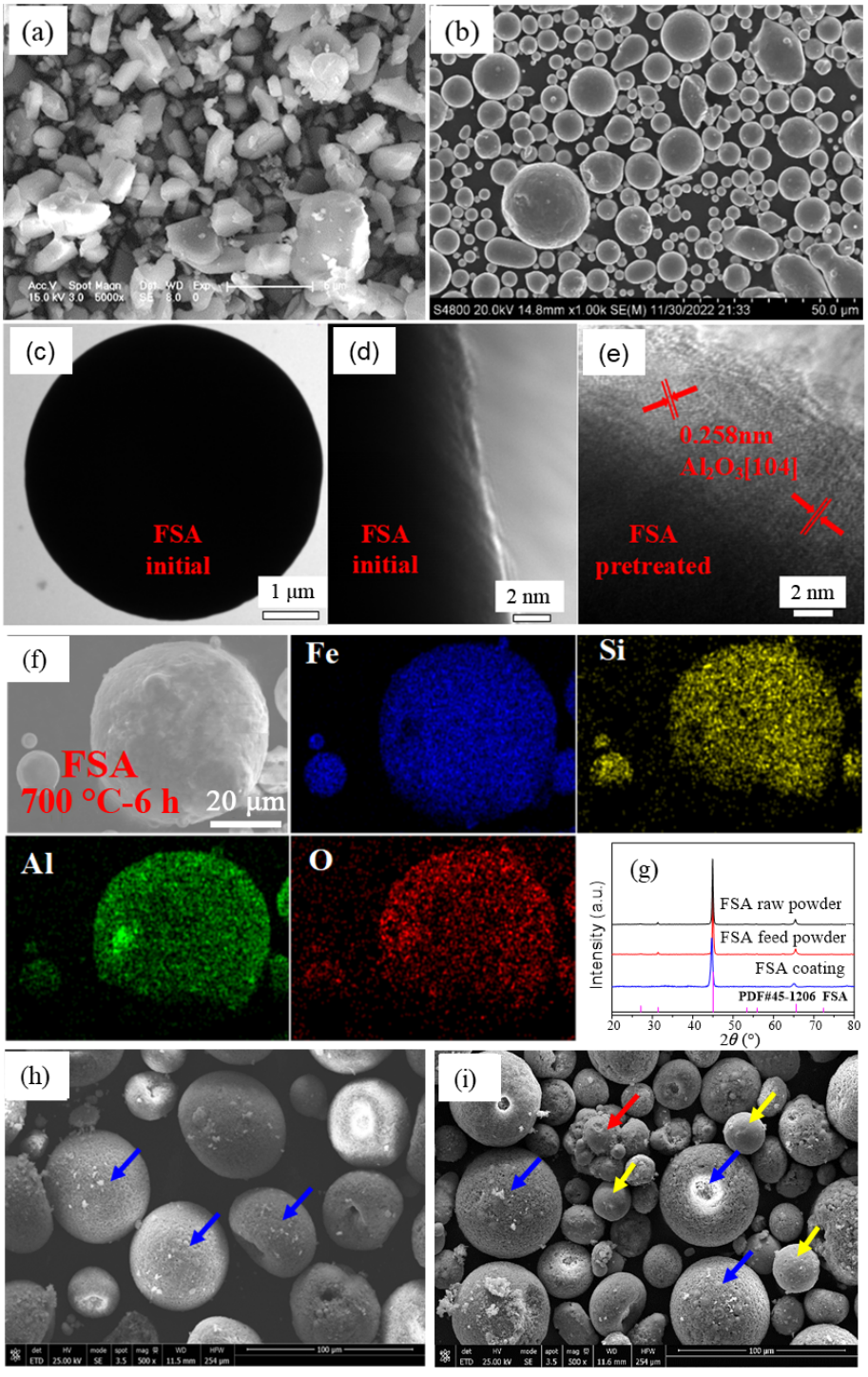

Fig. 1 SEM images of (a) produced LMA powder and (b) commercial FSA powder. (c) TEM image of commercial FSA powder and HRTEM images of (d) commercial FSA powder and (e) pretreated FSA powder. (f) SEM and EDS mappings of pretreated FSA powder at 700 °C. (g) XRD patterns of raw FSA powder, FSA feed powder, and FSA coating. SEM images of LMA–FSA composite feed powder with FSA contents of (h) 30 wt% and (i) 50 wt%, respectively.

3.2 EMW absorption of FSA powder and LMA thermal barrier ceramic powder

Good absorbing materials should satisfy two characteristics: (1) electromagnetic matching characteristics (RL), namely reducing reflection of incident EMW and maximum access to the interior of materials; (2) attenuation characteristics (α), namely effective absorption of EMW incident in space [7,30,44].

Figure 5(a) shows the curves of electromagnetic parameters ε', ε'', μ', and μ'' for the single FSA powder. The values of ε' and ε'' fluctuate around 8.85 and 0.15, respectively, which do not change obviously with frequency. The values of μ' and μ'' are about 2.06 and 1.07 at 2 GHz, respectively, and decrease with frequency increasing. As known, if the value of ε' is too high, the materials will present electromagnetic shielding, but if the value of ε' is too low, the materials will present wave transmission. Clearly, ε' value of FSA powder is in the moderate range of 3–15 [7,44]. Commonly, ε'' and μ'' account for the energy loss dissipative mechanism [30]. In contrast, the value of μ'' of FSA powder is much larger than that of ε''. Moreover, the dielectric loss tangent

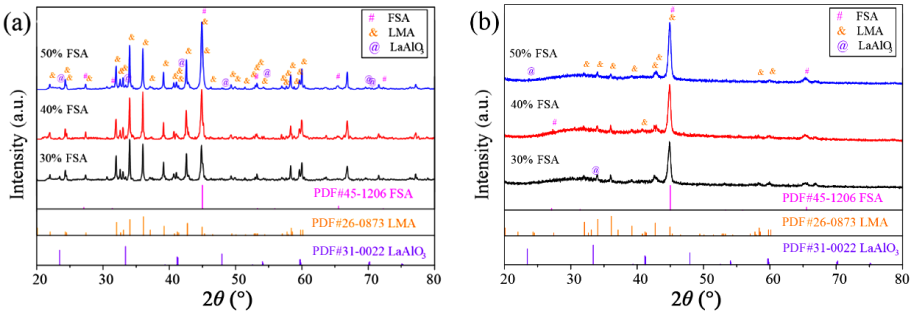

Fig. 2 XRD patterns of LMA ceramic composites: (a) feed powder and (b) APS coatings with different FSA contents.

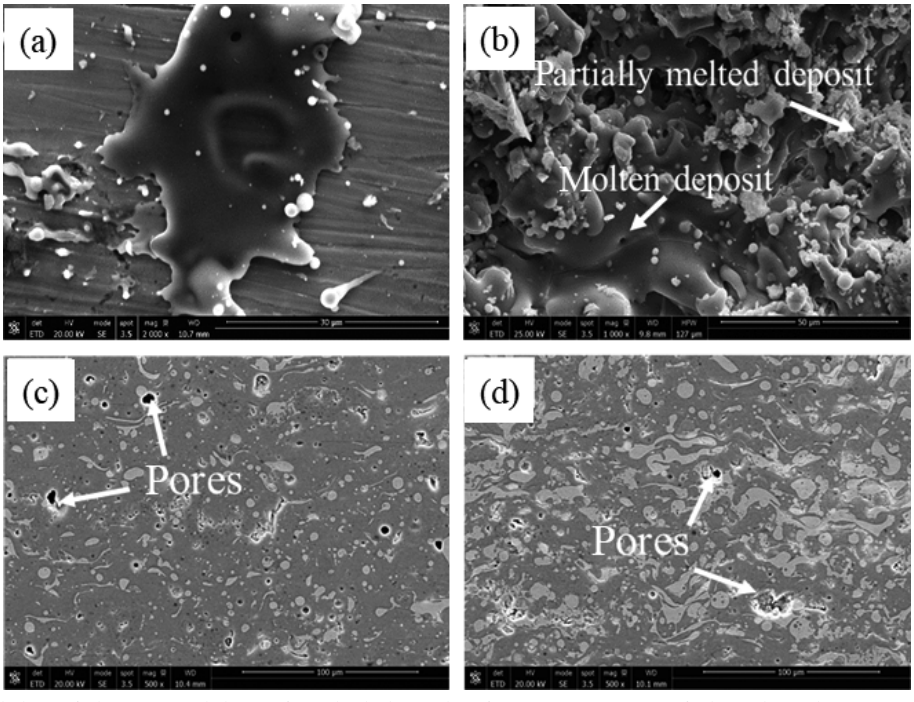

Fig. 3 (a) Typical morphology of plasma-sprayed deposit for individual particles of LMA–FSA composite feed powder and microstructures on (b) surface and (c, d) cross-sections of LMA–FSA composite TBCs with FSA contents of (b, c) 30 wt% and (d) 50 wt%, respectively.

is only about 0.01–0.04, while the magnetic loss tangent is up to 0.3–0.7 (Fig. 5(b)). All these indicate the mechanism of magnetic loss absorption of FSA powder. As shown in Fig. 5(c), the attenuation constant of FSA powder first increases and then decreases with frequency, and has a maximum value of about 192 at 12.24 GHz. From Fig. 5(d), RL has a minimum of −49.8 dB, and the EAB of RL < −10 dB is up to 5.66 GHz at a simulated thickness of 2 mm and frequency of 11.0 GHz. The EAB of RL < −10 dB covers almost the entire band of 4–18 GHz at simulated thicknesses of 1.5–3.0 mm. Figure 5(e) shows curves of the relative input impedance (Z_{in}/Z_0) with frequency at different thicknesses. As shown, the impedance matching factor is very close to 1 at the frequencies where RL has the minimum values for different simulated thicknesses (Fig. 5(d)). Obviously, it can be concluded that the FSA powder has excellent impedance-matching characteristics. However, the band of RL < −10 dB shifts to the low-frequency range of 2.0–6.5 GHz, and the impedance matching performance becomes relatively poor after plasma spraying of the FSA powder (Fig. S5 in the ESM).

Figure 6(a) shows the variations in ε', ε'', μ', and μ'' with frequency for the produced LMA thermal barrier ceramic powder. The electromagnetic parameters hardly change with the frequency at 2–18 GHz. The values of ε' and μ' are about 5.0 and 1.0, respectively, and those of ε'' and μ'' are close to zero. The dissipation capacity of materials to EMW energy mainly depends on the imaginary parts of permittivity and permeability, i.e., ε'' and μ'' [30]. From Fig. 6(b), the values of RL hardly exceed −2 dB at the entire band when the simulated thicknesses are 1.0–3.0 mm, indicating a poor EMW absorption performance. Obviously, the single LMA thermal barrier ceramic powder is difficult to be used as a microwave-absorbing material. In order to adjust the electromagnetic parameters of LMA, FSA powder could be introduced into the matrix of LMA ceramics as the microwave-absorbing agent.

3.3 EMW absorption of LMA–FSA composite feed powder

The absorbing property of materials may change after high-temperature melting and flattening spreading deposition during APS process. In order to study the heredity of EMW absorption of feed powder for APS, the absorbing properties of the LMA–FSA feed powder were studied first, and then those of the APS coatings.

Figures 7(a)–7(d) show electromagnetic parameters ε', ε'', μ', and μ'' of LMA–FSA composite feed powder with different FSA contents. From Fig. 7(a), the value of ε' increases with an increase

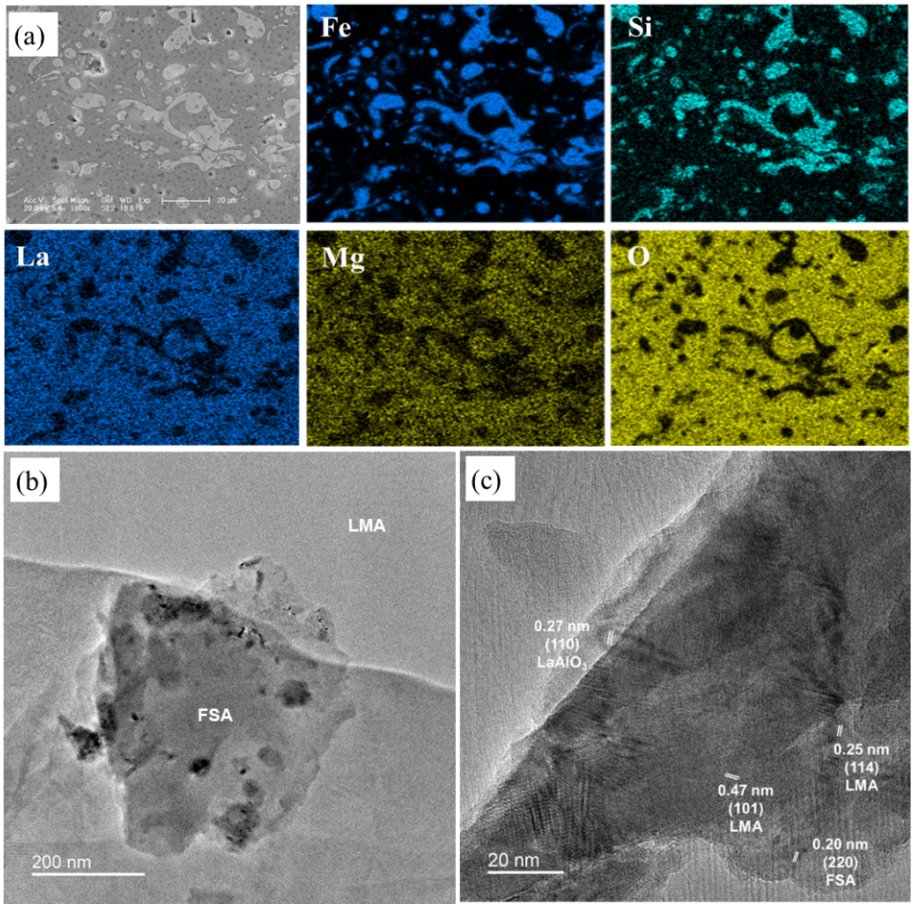

Fig. 4 (a) SEM and corresponding EDS mapping analysis of elements. (b) TEM image and (c) HRTEM image for LMA–FSA composite TBC with 40 wt% FSA.

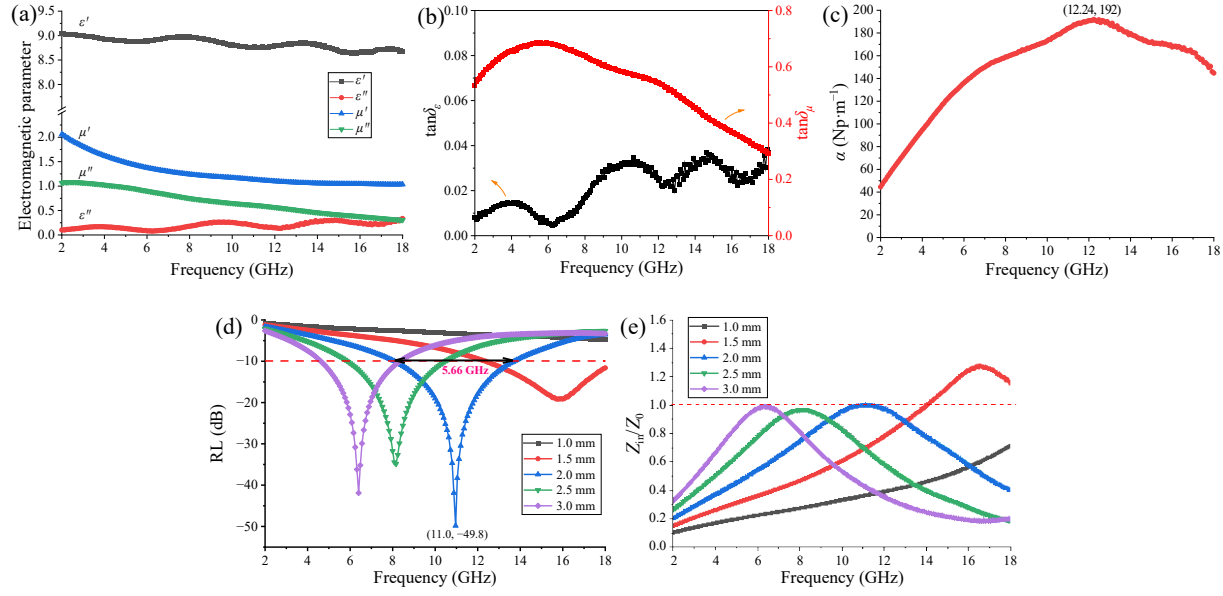

Fig. 5 Variations in (a) electromagnetic parameters ε', ε'', μ', and μ'', (b) $\tan\delta_\varepsilon$ and $\tan\delta_\mu$, (c) α, (d) RL, and (e) Z_{in}/Z_0 with frequency at 2–18 GHz for FSA powder.

in FSA content, and hardly changes with the increase of frequency, which fluctuates around 5.1, 5.5, and 5.9 for 30, 40, and 50 wt% FSA samples, respectively. Obviously, the real parts of permittivity of LMA–FSA composite feed powder are between those of single FSA powder and LMA powder. From Fig. 7(b), the imaginary parts of permittivity (ε'') change little with the FSA content and have no significant change compared with a single FSA powder. From Fig. 7(c), the value of μ' increases from 1.24 to 1.44 at 2 GHz with FSA content increasing from 30 to 50 wt%, and all decrease to about 1.0 with the increase of frequency. Figure 7(d) shows that the value of μ'' increases from 0.17 to 0.33 at 2 GHz with FSA content increasing from 30 to 50 wt%, and has an increasing trend with frequency increasing to 6 GHz, but then decreases with the frequency further increasing. Figures 7(e) and 7(f) show that $\tan\delta_\varepsilon$ is close to zero for all samples, while $\tan\delta_\mu$ is relatively much larger and increases significantly with an increase

in FSA content, implying that the absorbing loss mechanism of LMA–FSA feed powder belong to the magnetic loss type, and the loss is controlled by the content of FSA. As known, FSA is a magnetic absorbing agent [29–33], which essentially determines the magnetic loss mechanism of LMA–FSA composite feed powder. It is not difficult to find that the addition of FSA obviously improves the electromagnetic parameters of LMA powder. By contrast, the variation trend of electromagnetic parameters with frequency (Fig. S6(a) in the ESM) for the common Al_2O_3–FSA system is basically the same as that for the LMA–FSA system, but the dielectric constant of Al_2O_3–FSA system is obviously larger.

Figure 8 shows the variations in RL with frequency for LMA–FSA feed powder with different FSA contents at simulated thicknesses of 1.0–3.0 mm. Compared with single LMA powder (Fig. 6(b)), the curves of RL have much wider absorption peaks, which become stronger and shift to lower frequency with simulated thickness increasing. An increase in FSA content significantly decreases the value of RL at the same simulated thickness and frequency. The minimum values of RL (RL_{min}) for

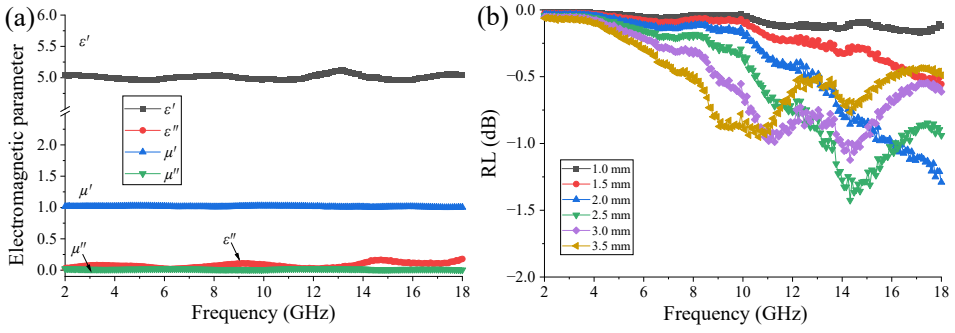

Fig. 6 Variations in (a) electromagnetic parameters ε', ε'', μ', and μ'' and (b) RL with frequency at 2–18 GHz for LMA thermal barrier ceramic powder.

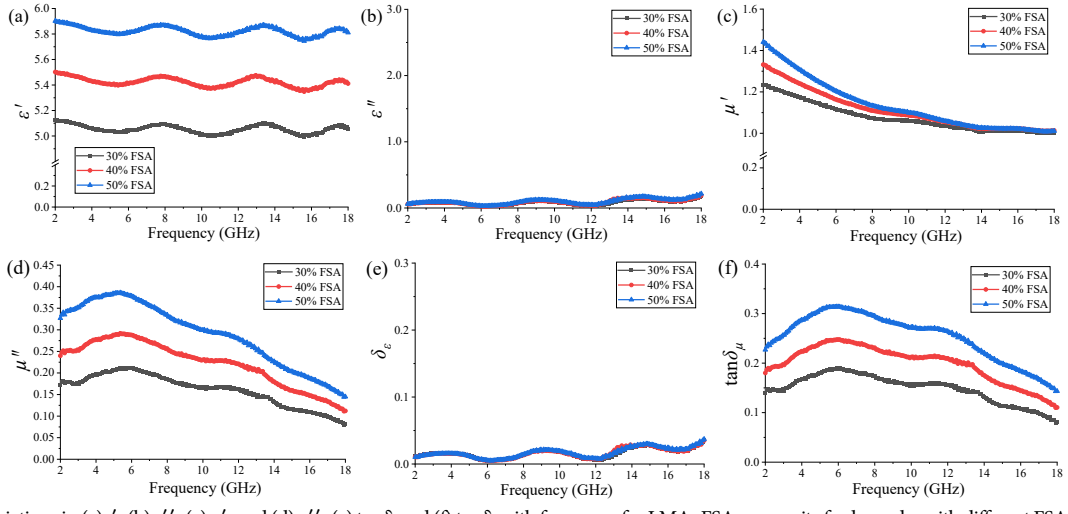

Fig. 7 Variations in (a) ε', (b) ε'', (c) μ', and (d) μ''. (e) $\tan\delta_\varepsilon$ and (f) $\tan\delta_\mu$ with frequency for LMA–FSA composite feed powder with different FSA contents.

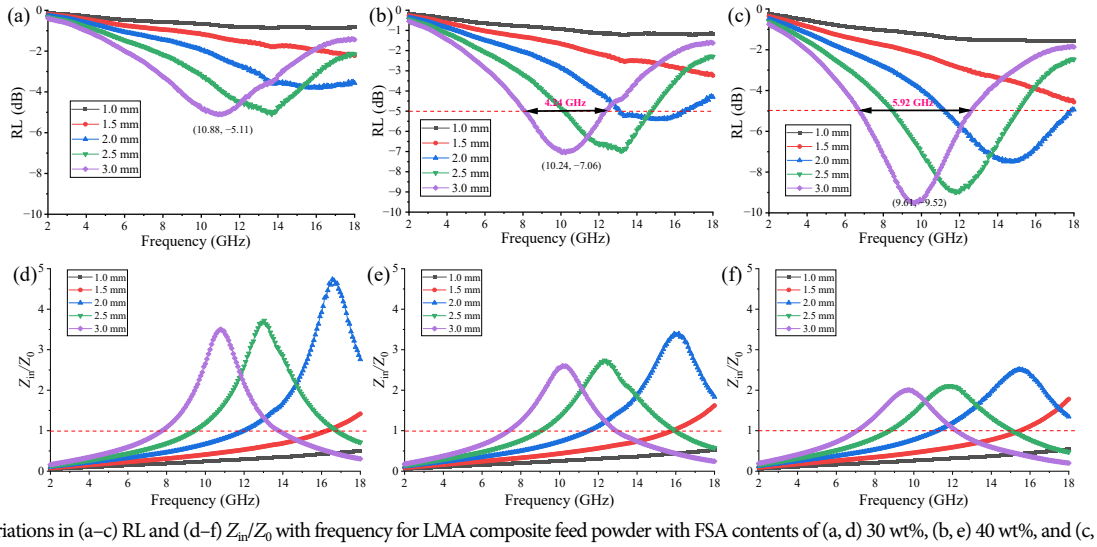

Fig. 8 Variations in (a–c) RL and (d–f) Z_{in}/Z_0 with frequency for LMA composite feed powder with FSA contents of (a, d) 30 wt%, (b, e) 40 wt%, and (c, f) 50 wt%.

清華大學出版社 Tsinghua University Press | SciOpen

30, 40, and 50 wt% FSA are −5.11, −7.06, and −9.52 dB at frequencies of 10.88, 10.24, and 9.61 GHz and simulated thickness of 3 mm, respectively. Obviously, RL_{min} for all samples are larger than −10 dB at simulated thicknesses of 1.0–3.0 mm. The curves of the relative input impedance (Z_{in}/Z_0) with different thicknesses are updated at 2–18 GHz for LMA composite feed powder with different FSA additions, as shown in Figs. 8(d)–8(f). The difference between the maximum value of Z_{in}/Z_0 and the ideal value of 1 becomes smaller and smaller with increasing the FSA addition content, indicating that the impedance matching of LMA ceramic powder is significantly improved by the addition of FSA. RL curves for Al_2O_3–FSA composite powder with 50 wt% FSA are shown in Fig. S6(b) in the ESM. In contrast, the value of RL for Al_2O_3–FSA system was relatively smaller than that for LMA–FSA system at the same frequency and simulated thickness.

Figure 9(a) shows the curves of attenuation constant (α) of LMA–FSA composite feed powder with different FSA contents. The value of α for all samples increases first and then decreases with frequency, which is the same as that of FSA powder. Moreover, an increase in FSA content results in an increase of α. The larger the imaginary part (μ'') of complex permeability is, the better the magnetic loss ability is [26]. As mentioned above, the value of μ'' increases with FSA content increasing (Fig. 7(d)). In fact, as shown in Fig. 9(b), the maximum saturation magnetization of the LMA–FSA feed powder is determined by the content of FSA, and the higher the FSA content, the higher the saturation magnetization, which thus resulted in much larger values of μ'' and α. According to Eq. (7), the value of α is inversely proportional to the value of μ' while directly proportional to the value of μ''. In Fig. 7(c), the value of μ' first decreases significantly with an increase in frequency and then decreases very slowly after 12.24 GHz, while the value of μ'' first increases and then decreases with the frequency increasing (Fig. 7(d)). Therefore, the curves of attenuation constant in Fig. 9(a) first display an increase and then a decrease with frequency increasing. The maximum values of α for LMA–FSA composite feed powder with 30, 40, and 50 wt% FSA are found to be 43.7, 61.2, and 80.1 Np·m^{-1} at 12.24 GHz, respectively.

3.4 EMW absorption of LMA–FSA composite coatings

The coatings were ground into powder to test the electromagnetic parameters, and the results are shown in Fig. 10. As indicated, the variation trends in ε', ε'', μ', μ'', and $\tan\delta_\varepsilon$, and $\tan\delta_\mu$ are basically the same as those of the feed powder (Fig. 7), but the electromagnetic parameters increased, namely the values of ε', ε'', μ', and μ'' of the coatings are obviously larger than those of the feed powder. As shown in Fig. 10(a), the values of ε' for LMA–FSA coatings with 30, 40, and 50 wt% FSA fluctuate around 6.6, 6.9, and 8.4, respectively. It is well known that the dielectric constant of composites is proportional to the quantity of charge stored on the surface [45]. As FSA content increased, FSA/LMA interfaces increased. Thus, a great deal of charge forms due to the polarization of the FSA/LMA interfaces [34]. Therefore, the higher value of ε' can be obtained with higher FSA content. The typical layered lamellae structure of coatings (Fig. 3) can form more interfaces of LMA/FSA than the spherical structure of the feed

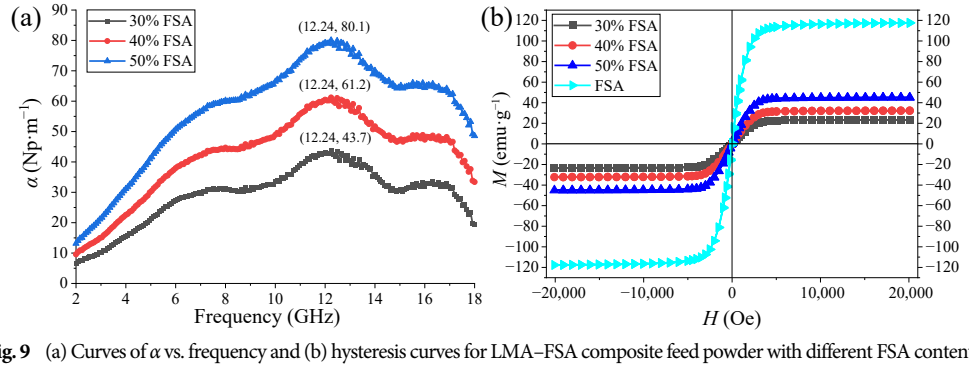

Fig. 9 (a) Curves of α vs. frequency and (b) hysteresis curves for LMA–FSA composite feed powder with different FSA contents.

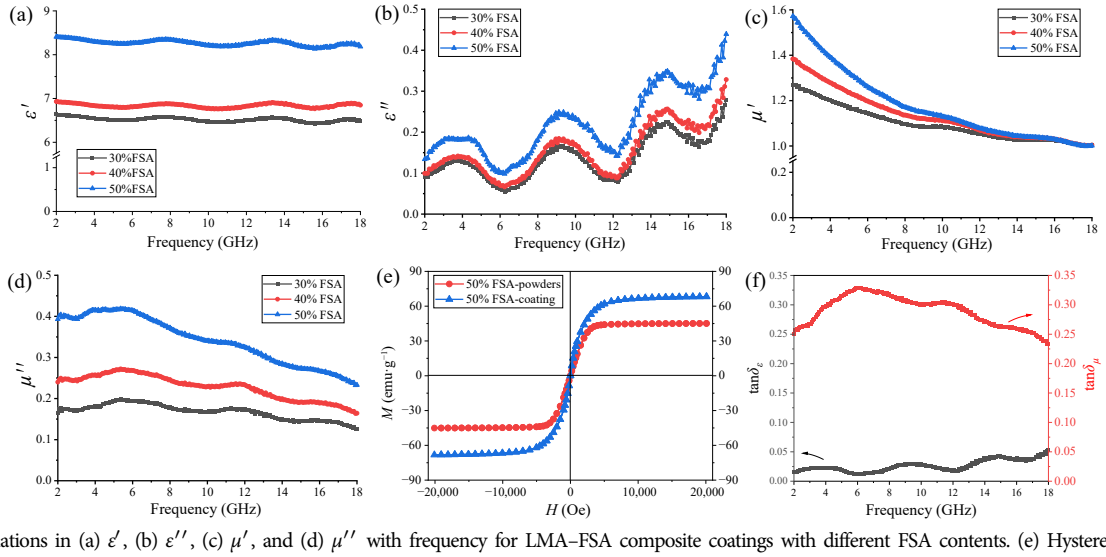

Fig. 10 Variations in (a) ε', (b) ε'', (c) μ', and (d) μ'' with frequency for LMA–FSA composite coatings with different FSA contents. (e) Hysteresis curves of LMA–FSA feed powder and coating, and (f) curves of $\tan\delta_\varepsilon$ and $\tan\delta_\mu$ of LMA–FSA composite coating with 50 wt% FSA.

powder, and the interface bonding is closer, which also resulted in an increase in ε' and ε'' after plasma spraying of the feed powder. It can be seen that the values of μ' and μ'' of LMA–FSA composite coatings with 30, 40, and 50 wt% FSA at 2 GHz are 1.27, 1.38, and 1.57 (Fig. 10(c)), and 0.17, 0.25, and 0.40 (Fig. 10(d)), respectively. The values of μ' and μ'' increased with FSA content increasing, which are consistent with the changes of the saturation magnetization with FSA content (Fig. 9(b)). In fact, the saturation magnetization of LMA–FSA composite coating increased significantly after plasma spraying of feed powder (Fig. 10(e)). For the isotropic spherical absorbent, the product between the magnetic resonance frequency and the initial permeability is approximately a constant, that is, Snoek's limitation, which can be represented by Eq. (8) [46], indicating that Snoek's limitation is related to the saturation magnetization.

$$f_r\left(\mu_i - 1\right) = \gamma M_s/3\pi \tag{8}$$

where f_r is the resonance frequency; μ_i is the initial permeability; γ is the rotatory magnetic ratio; M_s is the saturation magnetization. The relationship between the initial permeability and the resonance frequency changes greatly with the change in the absorber morphology [46]. For the flaky particles or films, the Snoek's limitation can be represented by Eq. (9) [46]:

$$f_r^2\left(\mu_i - 1\right) = (\gamma M_s/2\pi)^2 \tag{9}$$

According to Eqs. (8) and (9), LMA–FSA composite coating has a greater Snoek's limitation than the corresponding feed powder because, on the one hand, the saturation magnetization of the coating is greater than that of the feed powder (Fig. 10(e)), and on the other hand, the coating has a flat sheet stacking structure (Fig. 3). As a result, the complex permeability of coatings is relatively greater than that of the corresponding feed powder. In addition, the saturation magnetization of the coating increases as the content of FSA increases, and thus the Snoek's limitation and permeability of the coating also increase according to Eq. (9), which is consistent with the results of the complex permeability data (Figs. 10(c) and 10(d)). Because FSA phase is mainly preserved with the lamellae structure in the coatings (Fig. 3), the larger magnetic loss tangent appears in LMA–FSA coatings as compared with $\tan\delta_\varepsilon$ (Fig. 10(f)), indicating that EMW absorbing mechanism of LMA–FSA composite coatings is still mainly controlled by the magnetic loss.

Figure 11(a) shows the curves of α at 2–18 GHz for LMA–FSA composite coatings with different FSA contents. As can be seen, the variations in α with frequency and FSA content are essentially the same as those of the feed powder (Fig. 9(a)). However, compared with the feed powder, the attenuation constant of the coatings increased obviously, thanks to the higher complex permeability and saturation magnetization of the coatings [34]. The maximum values of α of LMA–FSA composite coatings with 30, 40, and 50 wt% FSA are found to be 51.0, 69.8, and 107.1 Np·m^{-1} at 12.24 GHz, respectively. Figure 11(b) shows the variation in $f^{-1}\left(\mu'\right)^{-2}\mu''$ with frequency for LMA–FSA composite coatings. It is well known that magnetic loss is mainly composed of hysteresis loss, domain wall resonance, eddy current loss, and natural resonance [47]. The hysteresis loss usually occurs in a strong magnetic field because the response of the magnetization vector lags behind that of the external field, so the hysteresis loss can be ignored [48]. Domain wall resonance occurs mainly in multi-domain wall materials [48]. The eddy current loss and natural resonance can be determined by Eq. (10) [29]:

$$C_0 = \mu''\mu'^{-2}f^{-1} \tag{10}$$

where C_0 is defined as a function of the frequency and the real and imaginary parts of permeability. When the value of C_0 on the left of Eq. (10) does not change with the applied frequency, the magnetic loss only comes from eddy current loss, otherwise, the main mechanism of magnetic loss is natural resonance [26,29]. As shown in Fig. 11(b), the value of $\mu''\mu'^{-2}f^{-1}$, i.e., C_0, decreases significantly with an increase in frequency for the LMA–FSA composite coatings, implying that the natural resonance is the main mechanism of magnetic loss of coatings.

Figures 12(a)–12(c) show the curves of RL as a function of frequency for LMA–FSA composite coatings with different FSA contents. As indicated, the RL_{min} decreases with FSA content increasing and changes little as simulated thickness increases to more than 2 mm; the values of RL_{min} for LMA–FSA coatings with FSA contents of 30, 40, and 50 wt% are −6.2, −8.2, and −13.4 dB at frequencies of 14.8, 14.3, and 12.5 GHz, respectively. The bandwidths of RL < −5 dB at a simulated thickness of 2 mm for the above three samples are 3.68, 6.08, and 7.86 GHz, respectively. Only 50 wt% FSA coating appears in EAB bands of RL < −10 dB at simulated thicknesses of 2.0–3.0 mm, which fully covers the entire X-band; at the simulated thickness of 2 mm, the EAB bandwidth is up to 3.11 GHz. Figures 12(d)–12(f) show the curves of the relative input impedance (Z_{in}/Z_0) for LMA–FSA composite coatings with different FSA contents. Obviously, RL of coatings is much smaller, and thus, the impedance matching is much better than those of the feed powder under the same condition, which mainly resulted from the higher complex permeability of coatings [49]. Therefore, LMA–FSA coatings have better absorbing properties than feed powder in terms of both impedance matching characteristics and attenuation characteristics.

The heat-treatments of the LMA–FSA composite coating with 50 wt% FSA were carried out in a muffle furnace (KSL–1500X,

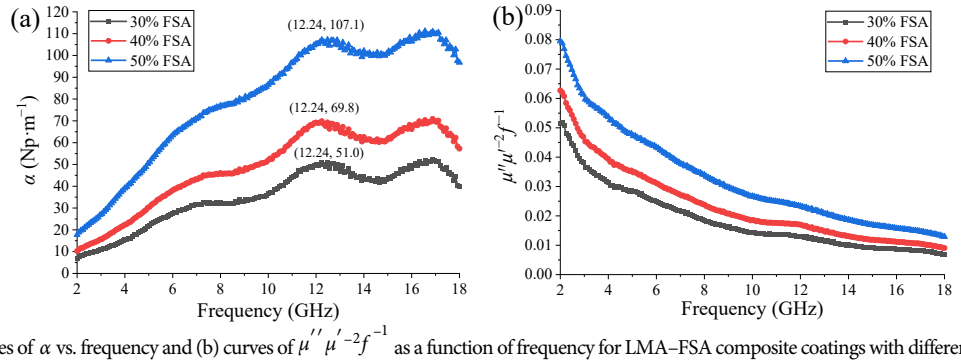

Fig. 11 (a) Curves of α vs. frequency and (b) curves of $\mu''\mu'^{-2}f^{-1}$ as a function of frequency for LMA–FSA composite coatings with different FSA contents.

清华大学出版社 Tsinghua University Press | SciOpen

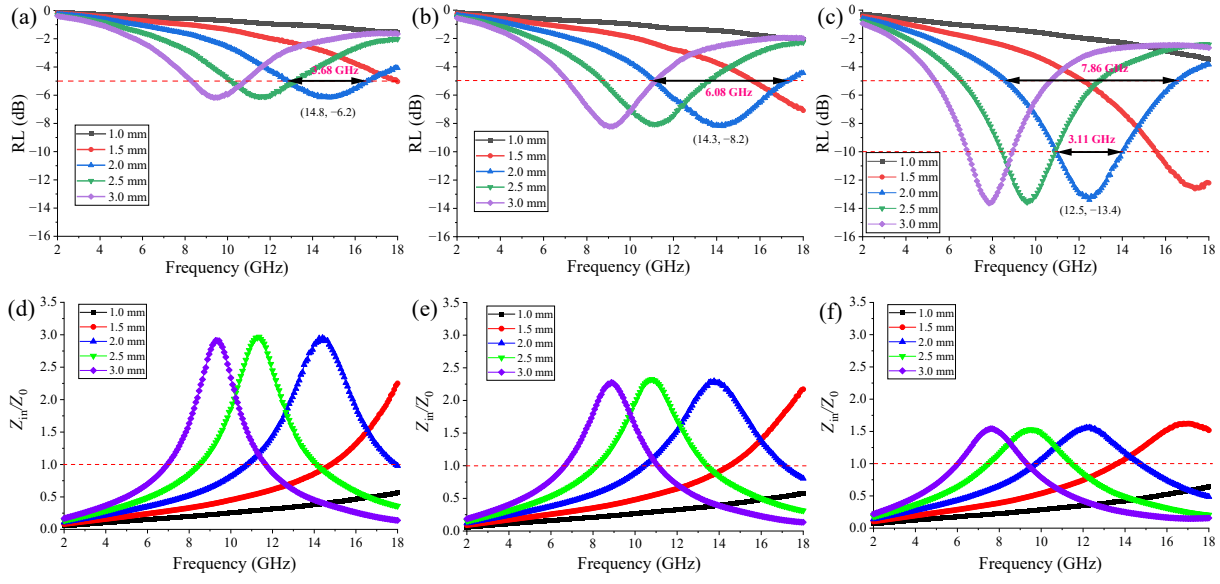

Fig. 12 Variations in (a–c) RL and (d–f) Z_{in}/Z_0 with frequency for LMA–FSA composite coatings with FSA contents of (a, d) 30 wt%, (b, e) 40 wt%, and (c, f) 50 wt%.

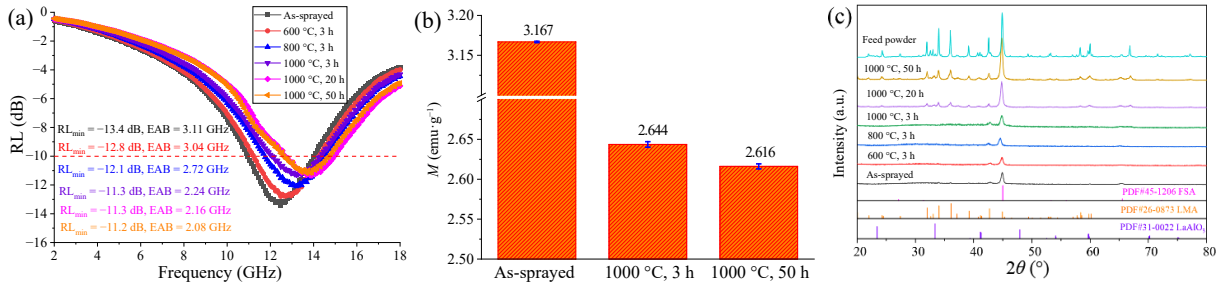

Fig. 13 (a) Curves of RL at simulated thickness of 2 mm for as-sprayed and heat-treated coatings at 600 °C for 3 h, 800 °C for 3 h, and 1000 °C for 3, 20, and 50 h. (b) Saturation magnetization of as-sprayed and heat-treated coatings at 1000 °C for 3 and 50 h and (c) XRD patterns of as-sprayed and heat-treated coatings and feed powder.

Hefei Kejing Material Technology Co., Ltd., China) at 600 °C for 3 h, 800 °C for 3 h, and 1000 °C for 3, 20, and 50 h, respectively. RL curves at a simulated thickness of 2 mm for the samples before and after heat treatments are shown in Fig. 13(a). It can be seen that the values of RL_{min} for as-sprayed and heat-treated coatings at 600, 800, and 1000 °C for 3 h are −13.4, −12.8, −12.1, and −11.3 dB, respectively, and those of the corresponding EAB (RL < −10 dB) are 3.11, 3.12, 2.72, and 2.24 GHz, respectively. Obviously, the value of RL_{min} increased, and that of EAB decreased with temperature increase. However, even after heat treatment at 1000 °C for 3 h, the value of EAB was still as high as 2.24 GHz. In addition, it was found that the values of RL_{min} and EAB for the heat-treated coatings at 1000 °C for 3, 20, and 50 h changed little. Figure 13(b) shows the saturation magnetization at a magnetic field of 100 Oe for the as-sprayed coating and heat-treated coatings at 1000 °C for 3 and 50 h. As indicated, the magnetic susceptibility of the as-sprayed coating is 3.167 emu·g^{-1}, and that of the heat-treated coating at 1000 °C for 3 h decreases to 2.644 emu·g^{-1}, while that of the further heat-treated coating at 1000 °C for 50 h almost unchanged with 2.616 emu·g^{-1}. Obviously, the change rule of magnetic susceptibility before and after heat treatment is consistent with that of RL_{min} and EAB, which is mainly due to the magnetic loss as the absorbing mechanism of the coatings. Figure 13(c) shows XRD patterns of LMA–FSA composite TBCs before and after heat treatments. It can be seen that XRD patterns of the coatings after heat treatment at 600, 800, and 1000 °C for 3 h are basically the same as that of the as-sprayed coating, but after heat treatment at 1000 °C for 20 and 50 h, the intensity of the diffraction peaks of XRD patterns is greatly enhanced, especially XRD pattern after heat-treatment for 50 h is basically consistent with that of the feed powder. The long-time heat-treatment at 1000 °C could result in sufficient amorphous recrystallization of APS coatings [38,39], and so the relative intensity of the diffraction peaks for the coating heated at 1000 °C for 50 h increased considerably. XRD results show that the phase composition of the heat-treated coatings has no obvious change and still remains the same as those of the feed powder, implying that LMA–FSA coatings have good phase stability during the heat treatment. As mentioned above, RL curves for the heat-treated coatings at 1000 °C for 3 and 50 h are very similar, and the values of RL_{min} and EAB do not differ greatly (Fig. 13(a)), implying that the amorphous recrystallization resulted from the heat-treatment has little effect on EMW loss property of TBCs. From Fig. 13, it is concluded that the phase and structure stability and microwave absorption properties of LMA–FSA composite TBCs could be relatively well preserved even after heat treatments at 600–1000 °C for 3–50 h.

3.5 Thermal properties of LMA–FSA composite coatings

Figure 14(a) shows the variation in thermal conductivity with temperature for LMA–FSA composite coatings with different FSA contents. It can be seen that the thermal conductivity increases with the FSA content and temperature increase. The thermal conductivities of 30 and 50 wt% FSA samples are about 2.84 and

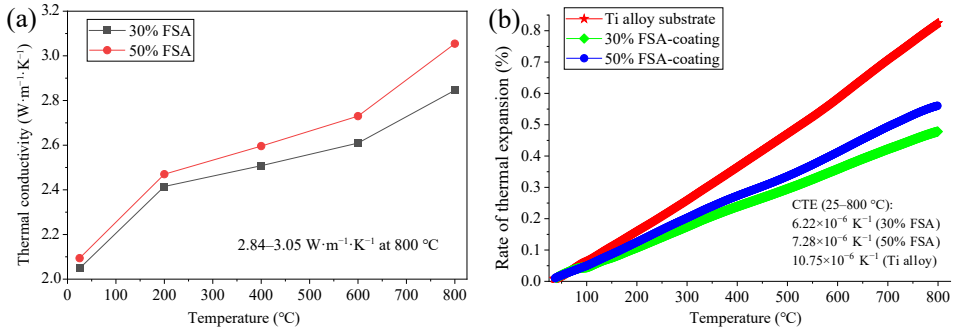

Fig. 14 Variations in (a) thermal conductivity and (b) rate of thermal expansion with temperature for as-sprayed LMA–FSA composite coatings with different FSA contents.

3.05 $W·m^{-1}·K^{-1}$ at 800 °C, respectively, indicating that the coatings could be used as potential TBCs for light alloys such as titanium alloy. Figure 14(b) shows the thermal expansion behavior of as-sprayed LMA–FSA composite coatings and titanium alloy, which increases almost linearly with temperature increasing. Coefficient of thermal expansion (CTE) at the temperature range can be obtained by linear fitting the curve of the temperature range [17]. The average CTEs of LMA–FSA composite coatings with FSA contents of 30 and 50 wt% and titanium alloy at 25–800 °C are about $6.22×10^{-6}$, $7.28×10^{-6}$, and $10.75×10^{-6}$ K^{-1}, respectively. Obviously, the thermal expansion mismatch between the coatings and titanium alloy is relatively small.

4 Conclusions

Single LMA powder has poor electromagnetic matching performance, which makes it difficult to use as microwave-absorbing material. However, microwave-absorbing functionalization of LMA composite TBCs was successfully realized by adding FSA absorber to LMA ceramic matrix to adjust the electromagnetic parameters. With the increase of FSA content from 30 to 50 wt%, EMW absorbing properties of LMA–FSA composite feed powder and coatings were both significantly improved. Due to the formation of layered lamellae structure during APS process, LMA–FSA composite coatings have better EMW absorbing properties than the corresponding feed powder. EMW absorption of LMA–FSA composite coatings is mainly controlled by the magnetic loss, and the natural resonance is the main mechanism of magnetic loss. LMA–FSA coatings exhibit a minimum RL value of −13.4 dB and the EAB of RL < −10 dB is up to 3.11 GHz at a simulated thickness of 2 mm. The EAB of RL < −10 dB covers the entire X-band at simulated thicknesses of 2.0–3.0 mm. The phase and structure stability and microwave absorption properties could be relatively well preserved even after heat treatments at high temperatures of 600–1000 °C. The average CTEs and thermal conductivity of LMA–FSA composite coatings are about $(6.22–7.28)×10^{-6}$ K^{-1} (25–800 °C) and 2.84–3.05 $W·m^{-1}·K^{-1}$ (800 °C), respectively.

Acknowledgements

This work is supported by Changchun Scientific and Technological Development Program (21ZY08) and National Natural Science Foundation of China (92060201). Sincerely thanks to Tianni Lu from Shenyang Aerospace University for his help in processing the absorbing data.

Declaration of competing interest

The authors have no competing interests to declare that are relevant to the content of this article.

Electronic Supplementary Material

Supplementary material is available in the online version of this article at https://doi.org/10.26599/JAC.2024.9220953.

References

[1] Padture NP, Gell M, Jordan EH. Thermal barrier coatings for gas-turbine engine applications. *Science* 2002, **296**: 280–284.
[2] Padture NP. Advanced structural ceramics in aerospace propulsion. *Nat Mater* 2016, **15**: 804–809.
[3] Feng J, Wang J, Yang KL, *et al.* Microstructure and performance of $YTaO_4$ coating deposited by atmospheric plasma spraying on TC4 titanium alloy surface. *Surf Coat Tech* 2022, **431**: 128004.
[4] Gu LJ, Chen XL, Fan XZ, *et al.* Improvement of thermal shock resistance for thermal barrier coating on aluminum alloy with various electroless interlayers. *Surf Coat Tech* 2011, **206**: 29–36.
[5] Fan XZ, Liu YJ, Xu ZH, *et al.* Preparation and characterization of 8YSZ thermal barrier coatings on rare earth-magnesium alloy. *J Therm Spray Techn* 2011, **20**: 948–957.
[6] Akinay Y, Gunes U, Çolak B, *et al.* Recent progress of electromagnetic wave absorbers: A systematic review and bibliometric approach. *ChemPhysMater* 2023, **2**: 197–206.
[7] Pang HF, Duan YP, Huang LX, *et al.* Research advances in composition, structure and mechanisms of microwave absorbing materials. *Compos Part B-Eng* 2021, **224**: 109173.
[8] Li Y, Qing YC, Yao HY, *et al.* A novel plasma-sprayed Ti_4O_7/carbon nanotubes/Al_2O_3 coating with bifunctional microwave application. *J Colloid Interf Sci* 2023, **645**: 165–175.
[9] Yao HY, Qing YC, Li Y, *et al.* Effect of B_4C content and annealing on complex permittivity and microwave-absorption properties of B_4C/Al_2O_3 coatings. *J Eur Ceram Soc* 2023, **43**: 1450–1458.
[10] Yang ZN, Luo F, Hu Y, *et al.* Dielectric and microwave absorption properties of TiAlCo ceramic fabricated by atmospheric plasma spraying. *Ceram Int* 2016, **42**: 8525–8530.
[11] Su JB, Zhou WC, Liu Y, *et al.* Effect of Ti_3SiC_2 addition on microwave absorption property of Ti_3SiC_2/cordierite coatings. *Surf Coat Tech* 2015, **270**: 39–46.
[12] Wang WC, Wang LY, Liu G, *et al.* Temperature-dependent dielectric properties and high-temperature microwave absorption performance of Ti_3SiC_2/Al_2O_3–13%TiO_2 coatings. *J Eur Ceram Soc* 2024, **44**: 254–260.
[13] Li R, Qing YC, Li W, *et al.* The electromagnetic absorbing properties of plasma-sprayed TiC/Al_2O_3 coatings under oblique incident microwave irradiation. *Ceram Int* 2021, **47**: 22864–22868.
[14] Liu Y, Wei SC, Tian HL, *et al.* Characterization of soft magnetic spinel ferrite coating prepared by plasma spray. *Surf Coat Tech* 2014, **258**: 189–199.
[15] Bobzin K, Bolelli G, Bruehl M, *et al.* Characterisation of plasma-sprayed $SrFe_{12}O_{19}$ coatings for electromagnetic wave absorption. *J Eur Ceram Soc* 2011, **31**: 1439–1449.
[16] Li J, Zhou D, Wang PJ, *et al.* Recent progress in two-dimensional materials for microwave absorption applications. *Chem Eng J* 2021, **425**: 131558.

[17] Huang P, Niu XD, Wang Y, *et al.* Ultra-broadband electromagnetic wave absorption of ceramic composite coating by atmospheric plasma spraying. *J Am Ceram Soc* 2023, **106**: 5832–8323.
[18] Wang S, Ashfaq MZ, Gong HY, *et al.* Electromagnetic wave absorption properties of magnetic particle-doped SiCN(C) composite ceramics. *J Mater Sci-Mater El* 2021, **32**: 4529–4543.
[19] Yang ZN, Luo F, Xu JS, *et al.* Dielectric and microwave absorption properties of $LaSrMnO_3/Al_2O_3$ ceramic coatings fabricated by atmospheric plasma spraying. *J Alloys Compd* 2016, **662**: 607–611.
[20] Zhou L, Zhou WC, Su JB, *et al.* Plasma sprayed Al_2O_3/FeCrAl composite coatings for electromagnetic wave absorption application. *Appl Surf Sci* 2012, **258**: 2691–2696.
[21] Zhao SX, Ma H, Li XQ, *et al.* Achieving high temperature broadband electromagnetic reflection reduction via Al_2O_3/FeCrAl refractory composite coating. *Ceram Int* 2022, **48**: 13340–13347.
[22] Zhou L, Su GX, Wang HB, *et al.* Influence of NiCrAlY content on dielectric and microwave absorption properties of NiCrAlY/Al_2O_3 composite coatings. *J Alloys Compd* 2019, **777**: 478–484.
[23] Qing YC, Zhou WC, Luo F, *et al.* Thin-thickness FeSiAl/flake graphite-filled Al_2O_3 ceramics with enhanced microwave absorption. *Ceram Int* 2017, **43**: 870–874.
[24] Cao XQ, Vassen R, Stoever D. Ceramic materials for thermal barrier coatings. *J Eur Ceram Soc* 2004, **24**: 1–10.
[25] Jia HY, Zhou WC, Nan HY, *et al.* Enhanced high temperature dielectric polarization of barium titanate/magnesium aluminum spinel composites and their potential in microwave absorption. *J Eur Ceram Soc* 2020, **40**: 728–734.
[26] Ma JB, Zhao B, Xiang HM, *et al.* High-entropy spinel ferrites MFe_2O_4 (M = Mg, Mn, Fe, Co, Ni, Cu, Zn) with tunable electromagnetic properties and strong microwave absorption. *J Adv Ceram* 2022, **11**: 754–768.
[27] Fang X, Jiang L, Pan LM, *et al.* High-thermally conductive AlN-based microwave attenuating composite ceramics with spherical graphite as attenuating agent. *J Adv Ceram* 2021, **10**: 301–319.
[28] Qiao LJ, Bi JQ, Liang GD, *et al.* Synthesis of high-entropy MXenes with high-efficiency electromagnetic wave absorption. *J Adv Ceram* 2023, **12**: 1902–1918.
[29] Zhang WM, Xiang HM, Dai FZ, *et al.* Achieving ultra-broadband electromagnetic wave absorption in high-entropy transition metal carbides (HE TMCs). *J Adv Ceram* 2022, **11**: 545–555.
[30] Elmahaishi MF, Azis RS, Ismail I, *et al.* A review on electromagnetic microwave absorption properties: Their materials and performance. *J Mater Res Technol* 2022, **20**: 2188–2220.
[31] Bobzin K, Öte M, Königstein T. Investigation of amorphous/nanocrystalline iron-based thermal barrier coatings. *J Therm Spray Techn* 2017, **26**: 388–397.
[32] Dong YQ, Liang XC, Zhong SJ, *et al.* A simple method for preparing flaky FeSiAl for low-frequency electromagnetic wave absorber. *J Magn Magn Mater* 2023, **574**: 170676.
[33] Cai XD, Jiang XJ, Xie W, *et al.* Effect of particle size on the preparation and microwave absorption properties of FeSiAl magnetically soft alloy hollow microspheres. *Def Technol* 2018, **14**: 477–483.
[34] Qing YC, Su JB, Wen QL, *et al.* Enhanced dielectric and electromagnetic interference shielding properties of FeSiAl/Al_2O_3 ceramics by plasma spraying. *J Alloys Compd* 2015, **651**: 259–265.
[35] Hu JW, Liu SC, Wang Y, *et al.* Manganese phosphate coated flaky FeSiAl powders with enhanced microwave absorbing properties and improved corrosion resistance. *Mater Chem Phys* 2023, **296**: 127274.
[36] Ye XC, Yang C, He EY, *et al.* Electromagnetic wave absorption properties of the FeSiAl/PLA and FeSiAl–MoS_2–graphene/PLA double-layer absorber formed by fused deposition modeling. *J Magn Magn Mater* 2023, **565**: 170280.
[37] Cao XQ, Zhang YF, Zhang JF, *et al.* Failure of the plasma-sprayed coating of lanthanum hexaluminate. *J Eur Ceram Soc* 2008, **28**: 1979–1986.
[38] Sun JB, Hui Y, Jiang JN, *et al.* Crystallization mechanism of plasma-sprayed $LaMgAl_{11}O_{19}$ coating. *Appl Surf Sci* 2020, **504**: 144509.
[39] Sun JB, Wang JS, Zhou X, *et al.* Microstructure and thermal cycling behavior of plasma-sprayed $LaMgAl_{11}O_{19}$ coatings. *Ceram Int* 2018, **44**: 5572–5580.
[40] Sun JB, Wang JS, Zhou X, *et al.* Thermal cycling behavior of the plasma-sprayed coating of lanthanum hexaaluminate. *J Eur Ceram Soc* 2018, **38**: 1919–1929.
[41] Lu XR, Yuan JY, Xu MY, *et al.* Improvement on thermophysical and mechanincal properties of $LaMgAl_{11}O_{19}$ magnetoplumbite by Nd_2O_3 and Sc_2O_3 co-doping. *Ceram Int* 2021, **47**: 28892–28903.
[42] Lu XR, Yuan JY, Li G, *et al.* Microstructures, thermophysical properties and thermal cyclic behaviors of Nd_2O_3 and Sc_2O_3 co-doped $LaMgAl_{11}O_{19}$ thermal barrier coating deposited by plasma spraying. *Ceram Int* 2022, **48**: 36539–36555.
[43] Zeng XJ, Jiang X, Ning Y, *et al.* Construction of dual heterogeneous interface between zigzag-like Mo–MXene nanofibers and small CoNi@NC nanoparticles for electromagnetic wave absorption. *J Adv Ceram* 2023, **12**: 1562–1576.
[44] Niu HH, Jiang XW, Xia YD, *et al.* Construction of hydrangea-like core–shell $SiO_2@Ti_3C_2T_x$@CoNi microspheres for tunable electromagnetic wave absorbers. *J Adv Ceram* 2023, **12**: 711–723.
[45] Qing YC, Zhou WC, Jia S, *et al.* Electromagnetic and microwave absorption properties of carbonyl iron and carbon fiber filled epoxy/silicone resin coatings. *Appl Phys A-Mater* 2010, **100**: 1177–1181.
[46] Snoek JL. Dispersion and absorption in magnetic ferrites at frequencies above one Mc/s. *Physica* 1948, **14**: 207–217.
[47] Xie S, Guo XN, Jin GQ, *et al.* Carbon coated Co–SiC nanocomposite with high-performance microwave absorption. *Phys Chem Chem Phys* 2013, **15**: 16104–16110.
[48] Li GM, Wang LC, Li WX, *et al.* $CoFe_2O_4$ and/or Co_3Fe_7 loaded porous activated carbon balls as a lightweight microwave absorbent. *Phys Chem Chem Phys* 2014, **16**: 12385–12392.
[49] Niu XD, Huang P, Wang Y, *et al.* Preparation and characterization of a composite ceramic coating containing absorber $LaFe_{12}O_{19}$ by plasma spraying. *Ceram Int* 2023, **49**: 27079–27085.